Journal of *Marine Science and Engineering*

MDPI

Article

Dynamic Modeling and Control of Floating Wind Turbine Platforms with a Gyroscopic Stabilizer

Ping Cheng [1,2,*], Tingyuan Zhang [1], Wenchuan Zhao [1] and Decheng Wan [2]

[1] College of Logistics Engineering, Shanghai Maritime University, Shanghai 201306, China; z15235417975@163.com (T.Z.); zwc970224@163.com (W.Z.)
[2] Computational Marine Hydrodynamics Lab (CMHL), School of Ocean and Civil Engineering, Shanghai Jiao Tong University, Shanghai 200240, China; dcwan@sjtu.edu.cn
* Correspondence: chengping@shmtu.edu.cn; Tel.: +86-18817893530

Abstract

A gyroscopic stabilizer generates an anti-roll moment by regulating the precession angle of a high-speed rotor. By computing the precession-angle command in real time, the controller can effectively suppress roll motion. However, research on the application of gyroscopic stabilizers to floating wind turbines remains limited. In this study, the operating mechanism of a gyroscopic stabilizer is modeled, and frequency-domain stability analyses are conducted for the system dynamics both before and after the installation of the stabilizer. A pole-placement-based controller is designed to achieve active stabilization of wave-induced platform motions by adjusting the rotor precession angle. Based on wave spectrum analysis, numerical simulations are performed to compare system responses with and without the active controller under different sea conditions. The results demonstrate that the proposed anti-roll control strategy exhibits robust performance and can increase the roll reduction rate by at least a factor of two across a range of sea states. In addition, the anti-roll effectiveness is influenced by rotor speed and environmental conditions, with higher reduction rates achieved at higher rotor speeds, larger wave heights, and longer wave periods. In addition, we adopt a dual-gyro configuration to cancel yaw-interference moments, and the proposed controller is feedback-based (platform motion only), which is suitable for retrofit applications without requiring wave-preview sensors.

Keywords: gyroscopic stabilizer; floating wind turbine; dynamic control

Academic Editor: Rodolfo T. Gonçalves

Received: 5 February 2026
Revised: 5 March 2026
Accepted: 6 March 2026
Published: 9 March 2026

1. Introduction

With the increasing scarcity of nonrenewable energy resources, renewable energy sources, particularly wind energy, have attracted growing attention. As key components for offshore wind power development in deep-water environments, floating wind turbines operate under complex and highly variable conditions. They are continuously subjected to wind and wave excitations, which induce roll and pitch motions of the platform [1]. These irregular swaying motions adversely affect the stability, seakeeping performance, and hydrodynamic resistance of floating wind turbine platforms [2].

For large-scale floating platforms, structural configuration and dynamic system characteristics are difficult to determine precisely. Under combined wind and wave loading, floating wind turbines may experience severe oscillations, leading to increased fatigue loads on structural and mechanical components. In extreme sea states, excessive platform motions can result in green water events or even capsizing, posing a serious threat to the

operational safety of floating wind turbines [3]. Therefore, effective suppression of platform swaying motions is essential for ensuring system safety and performance [4].

One feasible approach to mitigating roll motion in floating platforms is the application of relatively mature marine stabilization technologies. Conventional solutions, such as anti-roll water tanks, tuned mass dampers, and mooring anchor chains, are typically incorporated during the initial design stage of floating wind turbines. However, these methods are difficult to implement for platforms that have already been deployed offshore. In addition, anti-roll fins are ineffective at zero forward speed. Gyroscopic stabilizers, as a new type of anti-rolling device, have attracted increasing attention owing to their compact structure and ease of retrofitting on existing floating wind turbine platforms [5,6].

A gyroscopic stabilizer primarily utilizes the gyroscopic torque generated by a high-speed rotating rotor undergoing precession to suppress platform swaying. Its anti-rolling capability depends mainly on the rotor moment of inertia, rotational speed, and precession angular velocity. Depending on whether a precession-angle control system is utilized, gyroscopic stabilizers can be classified as passive or active types [7]. Palraj and Rajamanickam [8] installed an active gyroscopic stabilizer on a barge-type foundation equipped with a static tower and investigated gyroscopic performance at three rotor speeds. The results showed that, at high rotor speed, the maximum roll reduction rate reached 55% under regular waves and 54% under irregular waves. Based on this work, researchers subsequently installed a dynamic wind turbine on a static tower foundation and analyzed the damping performance of the gyroscopic stabilizer under different turbine rotor speeds. The results demonstrated that the gyroscopic stabilizer effectively suppressed roll and cross-roll motions induced by blade rotation [9].

In recent years, the active control capability of gyroscopic stabilizers has been significantly enhanced through the integration of sensors and control systems, enabling more effective suppression of floating wind turbine motions [10,11]. Perez and Steinmann [12] proposed a proportional–derivative (PD) control strategy in which the gyroscopic torque output was enhanced by adjusting the precession angular velocity of the universal joint, thereby improving the damping effect. Song et al. [13], inspired by passive gyroscopes without control systems, measured ship motion angles using attitude sensors and conducted experiments at different sampling frequencies. An angular-rate feedback control strategy combined with a proportional–integral–derivative (PID) algorithm was used to control gyroscope precession, achieving effective roll suppression in a ship model. Qi et al. [14] designed a PID-controlled gyroscope with fuzzy immune control for low-speed navigation conditions. Compared with a passive gyroscope, this device exhibited improved anti-rolling performance under random wave excitation.

Recent studies on wave-disturbance rejection increasingly exploit disturbance-preview information from upstream wave measurements (e.g., radar/LiDAR or vision-based wave sensing) and use predictive or feed-forward control to mitigate wave-induced motion and loads [15,16]. For example, Walker et al. developed nonlinear model predictive dynamic positioning with wave disturbance preview for ROV station keeping [17], and de Oliveira and de Barros proposed acceleration-based feedback/feedforward strategies under wave disturbance [18]. Wave-preview feedforward concepts have also been investigated for floating wind turbines (e.g., wave feedforward control in wave-tank experiments) [19]. In contrast, the present study focuses on a feedback-only gyrostabilizer controller that uses measured platform roll motion; the wave model is used only to generate simulation disturbances and is not required for online control [20].

At present, gyroscopic stabilizers have been widely applied to reduce ship roll motion. However, in the field of floating wind turbines, relatively limited research has been conducted on gyroscope-based anti-rolling mechanisms and control strategies [21]. In this

study, multibody dynamics modeling and numerical simulation are used to investigate the active control of a dual-gyro stabilizer installed on a floating wind turbine platform. The effects of active control, wave conditions, and gyro rotor speed on anti-rolling performance are analyzed. The main contributions of this study are as follows:

- A coupled roll–platform–dual-gyro dynamic model is established based on wave spectral theory, where the dual-gyro arrangement cancels yaw-interference moments and doubles the effective roll damping.
- The anti-rolling mechanism and the passive-versus-active stability characteristics of the gyrostabilizer are analyzed in the frequency domain, explicitly identifying additional resonance modes introduced by the gyro.
- A pole-placement-based gain-selection guideline for the feedback controller is derived, and time-domain simulations under irregular (JONSWAP) sea states are used to evaluate performance across rotor speeds and sea-state parameters. Practical implementation constraints (precession angle/rate limits) are also discussed.

The remainder of this paper is organized as follows. Section 2 presents the swaying motion model of the floating platform under wave excitation and explains the anti-rolling mechanism based on the gyroscope model, including parameter selection. Section 3 analyzes the frequency-domain stability of the platform with and without an active gyroscopic controller and introduces the controller design. Section 4 discusses the damping control responses under different rotor speeds and sea conditions. Finally, Section 5 concludes the paper.

2. Dynamic Model of the Platform in Waves

2.1. Wave Disturbance Model

Commonly used wave spectra, such as the Pierson–Moskowitz (PM) spectrum, mainly describe fully developed sea states, in which the duration and fetch of wind forcing are sufficiently long for the wave energy to reach equilibrium. However, in real ocean environments, waves are often in a developing or growing state owing to limited wind duration or fetch. Under these conditions, wave energy tends to be more concentrated around the peak frequency. By introducing a peak enhancement factor, the JONSWAP spectrum provides a more accurate representation of such sea states and better fits observed wave data. As a result, it has become an important tool in offshore engineering applications, including the design of North Sea oil platforms. Therefore, the JONSWAP spectrum is adopted in this study. The spectral density function expressed in terms of wind speed and fetch is given by

$$S_{\zeta}(\omega) = \frac{\alpha g^2}{\omega^5} e^{-\left(\frac{5\omega_0^4}{4\omega^4}\right)} \gamma^r, \tag{1}$$

where α is a dimensionless constant, ω_0 is the peak frequency, and γ is the peak enhancement factor. In Equations (1)–(4), g denotes gravitational acceleration; α is the (dimensionless) Phillips constant; ω_{p} is the peak angular frequency (related to the peak period T_p); and γ is the peak enhancement factor of the JONSWAP spectrum. In this revision, we consistently use γ (no γ').

The parameters α and ω_0 depend on the wind speed W_{10} and wind fetch F_{10}, and can be expressed as

$$\begin{aligned} \alpha &= 0.076\left(\frac{W_{10}^2}{F_{10}g}\right)^{0.22} \\ \omega_0 &= 22\left(\frac{g^2}{W_{10}F_{10}}\right)^{1/3}. \end{aligned} \tag{2}$$

The parameter r depends on the peak frequency ω_0 and the peak shape factor σ, and is defined as

$$r = e^{-\left[\frac{(\omega-\omega_0)^2}{2\sigma^2\omega_0^2}\right]}. \tag{3}$$

Alternatively, the JONSWAP spectrum can be expressed in terms of the significant wave height $\overline{H}_{1/3}$ as

$$\begin{aligned} S_\zeta(\omega) &= B_J \overline{H}_{1/3}^2 \frac{2\pi}{\omega}\left(\frac{\omega_0}{\omega}\right)^4 e^{-\left[\frac{5}{4}\left(\frac{\omega_0}{\omega}\right)^4\right]}\gamma^r \\ B_J &= \frac{0.06238}{0.230+0.0336\gamma-\frac{0.0185}{1.9+\gamma}}[1.094-0.01915\ln\gamma]. \end{aligned} \tag{4}$$

Under typical beam-sea conditions, the angle between the platform heading and the wave propagation direction is 90°. In this case, the wave encounter spectrum can be neglected.

By decomposing sufficiently long records of ocean wave data, the wave surface elevation can theoretically be represented as a superposition of an infinite number of sinusoidal wave components with different amplitudes, frequencies, and phases. Accordingly, the wave elevation can be expressed as

$$\zeta(x,t) = \sum_{i=1}^{n} h_i \cos(k_i x - \omega_i t + \varepsilon_i), \tag{5}$$

where k_i is the wave number, given by $k_i = {\omega_i}^2/g$ under deep-water conditions; h_i is the wave amplitude; and ε_i is the random phase, which follows a uniform distribution over $[0,\ 2\pi]$.

In this study, the equal-energy discretization method is adopted. Taking ω as the horizontal coordinate, the frequency range is divided into n subintervals $\omega_0,\ \omega_1,\ \ldots, \omega_n$ such that the spectral energy contained in each interval is equal. This condition can be expressed as

$$\int_{\omega_0}^{\omega_1} S_{\xi}(\omega)d\omega = \int_{\omega_1}^{\omega_2} S_{\xi}(\omega)d\omega = \ldots = \int_{\omega_{n-1}}^{n} S_{\xi}(\omega)d\omega, \tag{6}$$

where n is the number of equal-energy components. The representative frequency of each subinterval is determined by

$$\omega_i = \frac{\int_{\omega_{i-1}}^{\omega_i} \omega \cdot S_{\xi}(\omega)d\omega}{\int_{\omega_{i-1}}^{\omega_i} S_{\xi}(\omega)d\omega}, \quad i = 1,\ldots,n. \tag{7}$$

Accordingly, the wave elevation can be expressed as

$$\zeta(t) = \sum_{i=1}^{n} \sqrt{2S(\omega_i)\Delta\omega_i}\cos(k_i x - \omega_i t + \varepsilon_i) = \sum_{i=1}^{n} \sqrt{\frac{2\int_0^{\infty} S_{\alpha}(\omega)d\omega}{n}}\cos(k_i x - \omega_i t + \varepsilon_i). \tag{8}$$

Derivation note for Equation (8): the continuous spectrum S(ω) is approximated by n discrete components with equal energy, such that $\int_{\omega_{i-1}}^{\omega_i} \mathrm{S}(\omega)\mathrm{d}\omega = \mathrm{E}/\mathrm{n}$. For each band, the representative frequency ω_i is selected by Equation (7), and the corresponding component amplitude is computed as $A_i = \sqrt{2S(\omega_i)\Delta\omega_i}$, where $\Delta\omega_i = \omega_i - \omega_{i-1}$. The random phase φ_i is sampled from U~[0, 2π]. Substituting these discrete components into the Fourier superposition in Equation (5) yields Equation (8).

In the preceding discussion, wave amplitude was treated as the disturbance input. However, when analyzing the swaying motion of offshore platforms, it is necessary to consider the wave inclination angle as the system input. Converting the wave elevation spectrum into a wave inclination spectrum enables a more accurate representation of wave-induced swaying effects.

Under the assumption of linear, small-amplitude waves and a single-degree-of-freedom beam-sea condition, the relationship between wave elevation and wave inclination is given by

$$\begin{gathered} \alpha(t) = \frac{\partial \zeta}{\partial x} = k\zeta(t) = \sum_{i=1}^{n} k_i \sqrt{2S(\omega_i)\Delta\omega_i} \cos(k_i x - \omega_i t + \varepsilon_i) \\ S_\alpha(\omega) = \left[\frac{\omega^2}{g}\right]^2 S_\zeta(\omega) \end{gathered}, \tag{9}$$

where $S_\alpha(\omega)$ denotes the wave inclination spectrum.

2.2. Swing Model of the Platform

Compared with other angular motions of a floating wind turbine, swaying under beam-sea conditions can induce significant hazards through variations in the angle of attack, dynamic stall effects, and low-frequency motion amplification. Severe sea states can therefore adversely affect both the structural safety and power-generation stability of floating wind turbines. Hence, platform performance under beam-sea conditions is an important indicator for system evaluation. For generality, this study focuses on rolling motion as a representative case [22].

As shown in Figure 1, the floating wind turbine system is divided into two subsystems, including an upper subsystem consisting of the wind turbine and tower structure, and a lower subsystem comprising the floating support platform. A fully coupled aero-hydro-servo-elastic analysis of the entire system is highly complex. Because the roll motion considered in this paper is primarily induced by wave excitation acting on the floating support platform, we focus on the platform hydrodynamic roll response and neglect the coupled turbine/tower dynamics (including blade-induced gyroscopic effects) at this stage; this limitation is discussed in Section 4.4.

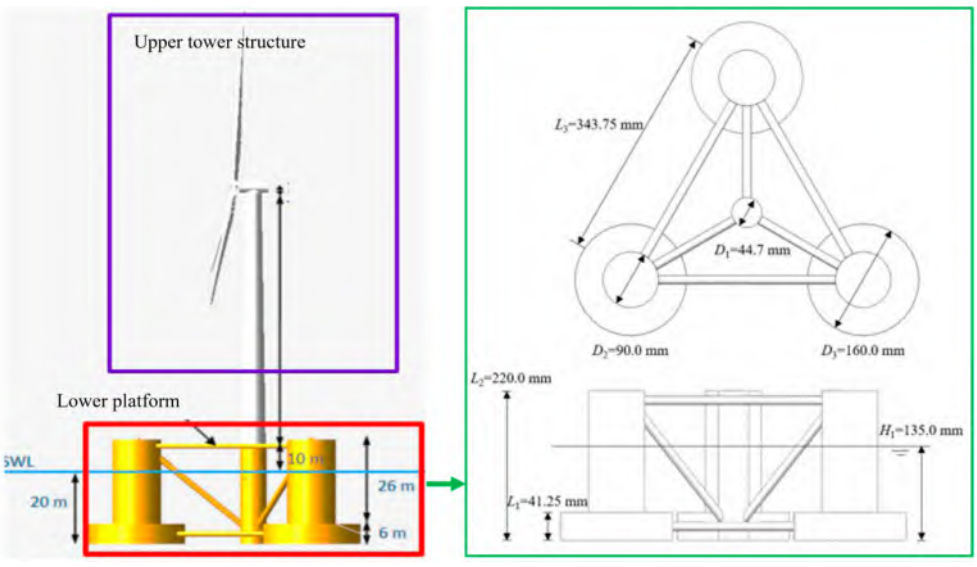

Figure 1. Full-scale floating wind turbine model (**left**) and top and side views of the scaled floating support platform (**right**).

To ensure the applicability of the gyroscopic stabilizer to floating wind turbines, the OC4 floating wind turbine platform, scaled by a factor of 1:50, is adopted as the simulation model. The main dimensions and configuration of the platform are shown in Figure 1. The geometric and inertial parameters of the platform before and after scaling are listed in Table 1. The 1:50 scale is adopted because OC4/DeepCwind at this scale is a widely used

public benchmark with extensive basin-test data and code-to-data validation materials. To avoid ambiguity, we also report full-scale equivalents of the key wave and gyro parameters using Froude similarity [23–25].

Table 1. Main dimensions of the full-scale and scaled floating platforms.

Model	L_1 (mm)	L_2 (mm)	L_3 (mm)	D_1 (mm)	D_2 (mm)	D_3 (mm)	H_1 (mm)	$\overline{GM}$ (mm)	m (kg)	I_{44}
Full-scale model	6000	32,000	50,000	6500	12,000	24,000	20,000	9740	1.40×10^7	1.56×10^{10}
Scaled model	41.25	220	343.75	44.7	90	160	135	135	111.64	49.76

The rolling motion of a floating platform in waves is inherently nonlinear owing to wave excitation and the platform's structural characteristics. To simplify the analysis, coupling effects from other degrees of freedom are neglected, and a single-degree-of-freedom nonlinear roll motion equation is established as

$$(I_{44} + a_{44})\ddot{\varphi} + B_{44}(\dot{\varphi}, \varphi) + D \cdot GZ(\varphi) = M(t), \tag{10}$$

where I_{44} is the roll moment of inertia of the platform, a_{44} is the added moment of inertia for the roll degree of freedom, and φ is the roll angle. $B_{44}(\dot{\varphi}, \varphi)$ denotes the roll damping moment, D is the platform displacement (weight), $GZ(\varphi)$ represents the restoring arm, and $M(t)$ is the wave-induced disturbance moment.

Justification of the 1-DOF roll model: the present study focuses on beam-sea, station-keeping conditions where the mean surge velocity is approximately zero. Under this operating regime, cross-coupled added-mass Coriolis terms that scale with products of translational velocities (e.g., terms proportional to u·v) are second-order small compared with the dominant hydrostatic restoring and wave-excited roll moment. In addition, the adopted semisubmersible platform is symmetric about the x–z plane, which further reduces first-order roll–sway coupling in the linearized hydrodynamic coefficients. These assumptions are consistent with the subsequent small-angle linearization from Equation (14) to Equation (15); when significant forward speed or strong multi-DOF coupling is present, a full 6-DOF model should be used. Extending the model to 6-DOF is therefore an important direction for future work [23].

The damping moment consists of a linear viscous damping term and a nonlinear quadratic damping term associated with frictional resistance and vortex shedding. It can be expressed as [26]

$$B_{44}(\dot{\varphi}, \varphi) = B_L\dot{\varphi} + B_N\dot{\varphi}\left|\dot{\varphi}\right|, \tag{11}$$

where B_L and B_N are the linear and nonlinear roll damping coefficients, respectively.

The restoring arm is approximated using a fifth-order polynomial expansion [27]:

$$GZ(\varphi) = C_1\varphi + C_3\varphi^3 + C_5\varphi^5, \tag{12}$$

where C_1, C_3, and C_5 are restoring moment coefficients.

The random wave-induced disturbance moment is expressed as a function of the wave inclination angle:

$$M(t) = D \cdot \overline{GM} \cdot \alpha(t), \tag{13}$$

where $\overline{GM}$ is the metacentric height associated with the platform's roll motion.

Substituting Equations (11)–(13) into Equation (10), the nonlinear roll motion equation under random wave excitation is obtained as

$$(I_{44} + a_{44})\ddot{\varphi} + B_L\dot{\varphi} + B_N\dot{\varphi}\left|\dot{\varphi}\right| + D\left(C_1\varphi + C_3\varphi^3 + C_5\varphi^5\right) = D \cdot \overline{GM} \cdot \alpha(t). \tag{14}$$

If the roll angle remains small (typically less than 10°), higher-order nonlinear terms can be neglected, and the roll motion equation can be approximated by a linear model:

$$(I_{44} + a_{44})\ddot{\varphi} + B_{44}\dot{\varphi} + C_{44}\varphi = D \cdot \overline{GM} \cdot \alpha(t), \tag{15}$$

where B_{44} is the linear roll damping coefficient, and C_{44} is the linear restoring moment coefficient.

2.3. Dynamics of the Gyrostabilizer

When waves act on the floating platform, they induce roll motion that generates a roll moment acting on the precession axis of the gyrostabilizer. This moment produces a precession torque τ_{prec}, which results in a precession angular velocity ω_{prec}. The precession motion, combined with the angular momentum of the gyroscope rotor, generates a gyroscopic torque τ_{gyro}. This torque acts in the transverse plane and opposes the wave-induced roll moment, thereby suppressing platform motion. This relationship can be expressed as

$$\tau_{\text{gyro}} = I\omega\omega_{\text{prec}}\,, \tag{16}$$

where I is the rotational inertia of the rotor, and ω is the rotor angular velocity.

Note on Equation (16): all quantities in the precession-rate bound are scalar magnitudes in this formulation; therefore, the dot notation for products is omitted in the revised equation.

The dynamic behavior of the gyrostabilizer is governed by classical gyroscope dynamics. In practical applications, the outer frame of the gyrostabilizer is rigidly connected to the hull. To accurately evaluate the output torque, the coordinate system shown in Figure 2 is introduced.

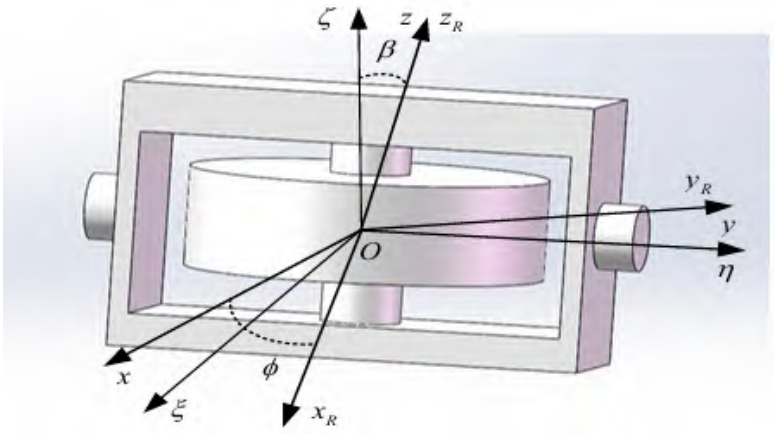

Figure 2. Anti-roll gyro coordinate system.

In the considered retrofit configuration, the dual-gyro module is rigidly bolted to the platform deck structure and aligned such that the rotor spin axes lie in the transverse plane while the precession axes are parallel to the platform roll axis. The module is placed as close as practicable to the platform center of mass to minimize additional static heel and to reduce structural loads transmitted to the deck. The dual-gyro arrangement is implemented within a single mechanical housing to ensure matched inertia and to minimize phase mismatch; remaining asymmetries (manufacturing tolerances, sensor bias, actuator delay) are discussed in Section 4 as implementation limitations.

The center O of the gyroscope rotor is taken as the origin of the inertial coordinate system $O - \xi\eta\zeta$, which is fixed to the hull and therefore also referred to as the hull coordinate system. By rotating this system about the $O - \zeta$ axis through an angle φ, the gyroscope

coordinate system $O-xyz$ is obtained. The gyroscope rotor spins at a constant angular velocity ω_0 about the $O-z$ axis, while the gyroscope frame undergoes precession about the $O-y$ axis.

The gyrostabilizer is assumed to be an axisymmetric rigid body with angular momentum $h_0 = I\omega$. The moment of inertia about the precession axis $O-y$ is denoted by J. The precession angle and angular velocity are represented by β and $\dot{\beta}$, respectively, while $\dot{\varphi}$ denotes the platform roll rate. The output torques of the gyrostabilizer in the ξ, η, and ζ directions of the $O-\xi\eta\zeta$ coordinate system can then be expressed as

$$\begin{cases} \mathrm{M}_\xi = I\omega\dot{\beta}\cos\beta \\ \mathrm{M}_\eta = J\ddot{\beta} - I\omega\dot{\varphi}\cos\beta \\ \mathrm{M}_\zeta = I\omega\dot{\beta}\sin\beta \end{cases}. \tag{17}$$

The derivation of these expressions is omitted here for brevity.

Equation (17) indicates that when the platform undergoes roll motion about the $O-\eta$ axis owing to wave excitation, the gyrostabilizer produces not only a damping moment M_ξ along the $O-\xi$ axis but also an interference moment M_ζ along the $O-\zeta$ axis. The latter affects the yaw motion of the platform. Moreover, the damping moment M_ξ varies with the cosine of the precession angle, whereas the interference moment M_ζ varies with the sine of the precession angle.

To eliminate the influence of the gyrostabilizer on the yaw degree of freedom, a dual-gyro configuration is adopted. In this configuration, two gyroscopes operate as a pair with equal rotational speeds in opposite directions. When external excitation occurs, the two gyroscopes undergo precession with equal magnitudes but opposite directions of angular velocity. Consequently, their output torques along the $O-\zeta$ axis are equal in magnitude and opposite in direction, resulting in mutual cancellation. At the same time, the damping torques along the $O-\xi$ axis are equal in magnitude and identical in direction, and therefore add constructively. This dual-gyro arrangement effectively cancels interference torques while amplifying the damping torque. The working principle is shown in Figure 3.

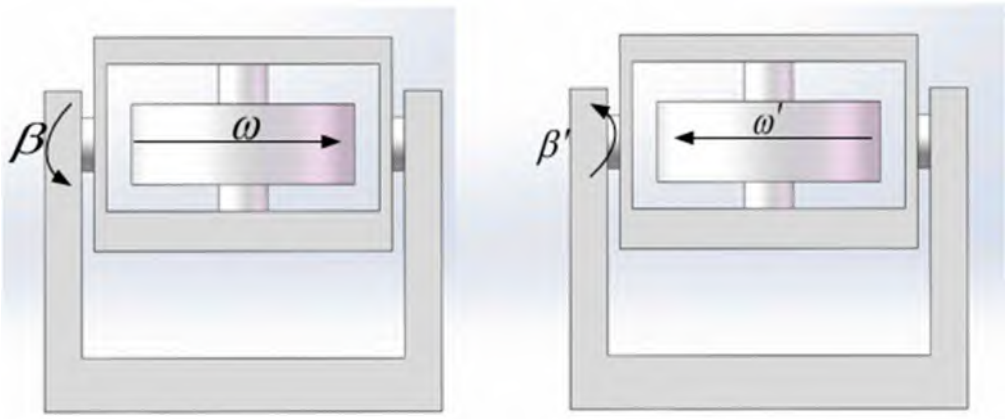

Figure 3. Schematic of the dual-gyro system model.

Let the rotational speeds of the two gyroscopes be ω and ω', and the corresponding precession angles be β and β', respectively. Neglecting coupling between roll motion and

other degrees of freedom, the dynamic equations in the $O-\xi\eta\zeta$ coordinate system can be written, based on Equation (17), as

$$\begin{cases} M'_{\xi} = I\omega\dot{\beta}\cos(\beta) - I\omega'\dot{\beta}'\cos(\beta') \\ M'_{\eta} = J\ddot{\beta} - I\omega\dot{\varphi}\cos(\beta) + J\ddot{\beta}' - I\omega'\dot{\varphi}\cos(\beta') \\ M'_{\zeta} = I\omega\dot{\beta}\sin(\beta) + I\omega'\dot{\beta}'\sin(\beta') \end{cases}. \tag{18}$$

Owing to the symmetry of the system, $\beta' = -\beta$ and $\omega' = -\omega$. Substituting these relations into Equation (18) gives

$$\begin{cases} M'_{\xi} = 2I\omega\dot{\beta}\cos(\beta) \\ M'_{\eta} = 0 \\ M'_{\zeta} = 0 \end{cases}. \tag{19}$$

Equation (19) confirms that, in the dual-gyro configuration, the damping moment acting along the $O-\xi$ axis is doubled, while the interference moments along the other axes are eliminated.

By incorporating the gyroscopic damping moment into the linear roll model given in Equation (15) and combining it with the gyroscope dynamics in Equation (17), a coupled mathematical model of the platform–gyrostabilizer system can be obtained:

$$\begin{cases} (I_{44} + a_{44})\ddot{\varphi} + B_{44}\dot{\varphi} + C_{44}\varphi = D\overline{GM}\cdot\alpha(t) - 2I\omega\dot{\beta}\cos(\beta) \\ J\ddot{\beta} = I\omega\dot{\varphi}\cos(\beta) + \tau_p \end{cases}, \tag{20}$$

where τ_p represents the input control torque.

Equation (20) indicates that the anti-rolling capability of the gyrostabilizer is directly related to its moment of inertia and rotational speed. Once the gyrostabilizer is designed, both the rotor inertia and the precession inertia are fixed, and the rotor speed remains constant during steady operation. Therefore, apart from the platform roll rate, the primary factor influencing the precession angular velocity is the applied control torque. Introducing an active control moment to regulate the precession motion is thus the primary mechanism for achieving active roll suppression.

2.4. Gyrostabilizer Parameter Selection

The selection of gyrostabilizer parameters is governed by the maximum wave-induced disturbance moment under extreme sea conditions, which corresponds to the maximum anti-rolling moment that the gyrostabilizer must provide. As this study focuses on a scaled model, the environmental parameters must first be scaled accordingly.

Scale models of offshore platforms are commonly designed based on the Froude similarity criterion. If the geometric scale ratio is defined as $\lambda = L_{full}/L_{model}$, the corresponding scale ratios for time and velocity are $\sqrt{\lambda}$ and $\sqrt{\lambda}$, respectively. Consistently, mass scales as λ^3, inertia as λ^5, force as λ^3, and moment as λ^4. Within the operating range of the floating platform, the JONSWAP spectrum in Equation (4) yields a significant wave height Hs = 6 m and a peak period Tp = 5.5 s for the full-scale condition. After scaling (λ = 50), these values become Hs = 0.12 m and Tp = 0.78 s at model scale; throughout Section 4 we report both model-scale inputs and their full-scale equivalents.

Based on Equation (4), the time history of the wave inclination angle $\alpha(t)$ can be obtained by inverse transformation. The corresponding wave-induced disturbance torque is then calculated using Equation (13). Its time history resembles zero-mean broadband (white-noise-like) excitation. The maximum value of this signal represents the limiting disturbance moment, and the maximum wave inclination angle is approximately 18°.

According to Equation (16), physical constraints impose an upper limit on the precession angular velocity, which is taken as $\dot{\beta}_{max} = 1.1$ rad/s. The rotor angular velocity is assumed to be constant at 3000 r/min. Under these conditions, the required rotational inertia of the rotor is calculated as

$$I = \frac{\tau_{\text{gyro}}}{\omega \cdot \dot{\beta}} = 0.013 \text{ kg·m}^2. \tag{21}$$

In addition, the rotational inertia of a solid cylindrical rotor can be expressed as

$$I = \frac{1}{2} m R^2, \; m = \rho \pi R^2 h, \tag{22}$$

where m, ρ, R, and h denote the mass, density, radius, and height of the rotor, respectively. Assuming the rotor is made of iron with a density of 7850 kg/m^3, the corresponding rotor radius and mass can be determined. The precession moment of inertia is taken as $J = 3.45 \times 10^{-3}$ kg·m^2. The main parameters of the dynamic model for the scaled floating platform and gyrostabilizer are listed in Table 2.

Table 2. Main parameters of the dynamic model of the scaled floating platform.

Parameter	a_{44}	B_{44}	C_{44}	I	J
Value	7.44 kg·m^2	6.5 N·m·s/rad	72.96 N·m/rad	0.013 kg·m^2	3.45×10^{-3} kg·m^2

2.5. Benchmark Consistency and Model Credibility

Although the present study is numerical, the OC4/DeepCwind semisubmersible geometry and mass properties adopted here are based on publicly documented benchmark definitions and scale-model test campaigns. Table 3 provides a brief consistency check by comparing key mass/inertia values with benchmark reports. This supports the credibility of the baseline (no-gyro) platform dynamics used for control design [23–25].

Table 3. Comparison of key mass/inertia values with benchmark reports.

Quantity	This Manuscript (Table 1)	Benchmark Source	Benchmark Value
Platform mass (kg)	1.40×10^7	Robertson et al., 2014 (OC4 definition) [22]	1.3473×10^7
System roll/pitch inertia about CM (kg·m^2)	~1.56×10^{10}	DeepCwind semisubmersible definition [25]	~(1.39–1.56) $\times 10^{10}$

3. System Stability Analysis and Controller Design

Monochromatic (sinusoidal) wave-inclination inputs are used in Section 3 only to interpret frequency-domain stability and resonance mechanisms. All performance evaluations in Section 4 use irregular waves synthesized from the JONSWAP spectrum (multi-component), consistent with North Sea sea-state descriptions.

3.1. Analysis of Passive Systems with a Gyrostabilizer

For the system dynamics given in Equation (20), the equations are linearized about the equilibrium point using the small-angle approximation $cos\beta \approx 1$. Applying the Laplace transform to Equation (20) gives

$$\begin{cases} \left[(I_{44} + a_{44})s^2 + B_{44}s + C_{44}\right]\varphi(s) = M(s) - 2I\omega s\beta(s) \\ Js^2\beta(s) = I\omega s\varphi(s) + \tau_p(s) \end{cases}. \tag{23}$$

When the gyrostabilizer is not considered, the system input is the wave-induced inclination $\alpha(s)$, and the output is the platform roll angle $\varphi(s)$. The open-loop transfer function of the platform is therefore

$$G(s) = \frac{\varphi(s)}{M(s)} = \frac{1}{(I_{44} + a_{44})s^2 + B_{44}s + C_{44}}, \tag{24}$$

where $M(s) = D\cdot\overline{GM} \cdot \alpha(s)$, and $D\cdot\overline{GM}$ is a constant.

When the active control torque $\tau_p(s)$ is neglected, the second equation in Equation (23) gives $\beta(s) = \frac{I\omega}{Js}\varphi(s)$. Thus, introducing the gyrostabilizer is equivalent to adding a feedback term with gain $H(s) = \frac{2(I\omega)^2}{J}$ to the original open-loop system. If first-order and second-order damping effects associated with gyroscope rotation are considered, the feedback transfer function becomes $H(s) = \frac{2(I\omega)^2 s^2}{Js^2 + B_{gyro}s + C_{gyro}}$. The corresponding block diagram of the platform system with the dual-gyro model is shown in Figure 4.

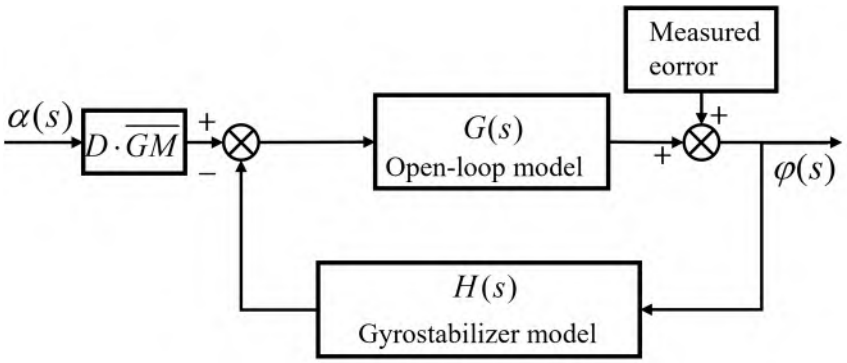

Figure 4. Structure diagram of the platform system with the dual-gyro model.

The closed-loop transfer function of the system after introducing the gyrostabilizer is given by

$$F(s) = \frac{\varphi(s)}{M(s)} = \frac{G(s)}{1 + G(s)H(s)}. \tag{25}$$

The rotational speed of the gyrostabilizer ω is assumed to be constant and is set to 1000, 3000, and 5000 rpm, respectively. The Bode plots of the original open-loop system and the corresponding closed-loop systems at these rotational speeds are shown in Figure 5.

As indicated by the blue curve, the original platform dynamics follow a second-order system. When the wave excitation frequency approaches the natural frequency of the platform, $\omega_\varphi \approx 1.13$ rad/s, the amplitude–frequency response increases significantly, resulting in resonance. Introducing the gyrostabilizer substantially reduces the response amplitude near this frequency; however, it also introduces additional resonance phenomena in both the low-frequency and high-frequency ranges.

As the gyroscope rotational speed increases, the additional resonant frequencies shift toward both lower and higher frequency bands. When the rotational speed approaches zero, the closed-loop response converges to that of the open-loop system. The high-frequency resonance is less pronounced because waves in this range typically correspond to short-period, low-amplitude, and low-energy disturbances, resulting in small response amplitudes. The increased response in the low-frequency range is potentially dangerous and is more likely to occur in offshore environments far from the coast. This behavior highlights the necessity of introducing an active controller. Without appropriate control compensation, the platform cannot operate safely under low-frequency wave conditions.

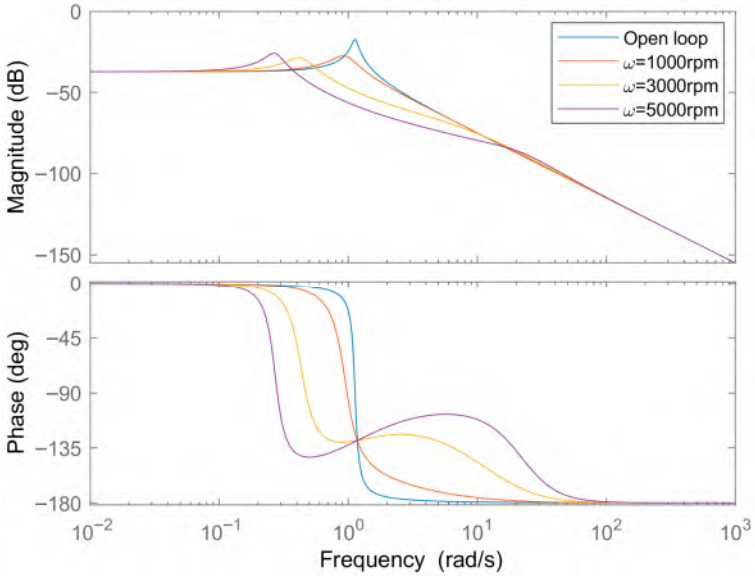

Figure 5. Bode plots of the original open-loop system and the three closed-loop systems at different rotational speeds.

For further investigation, the gyrostabilizer rotational speed is fixed at $\omega = 3000$ rpm, and the wave inclination $\alpha(t)$ is modeled as a sinusoidal input with frequencies of $0.1\omega_\varphi$, ω_φ, and $10\omega_\varphi$, respectively. The amplitude of $\alpha(t)$ is set to 10°. The corresponding time-domain simulation results are shown in Figure 6.

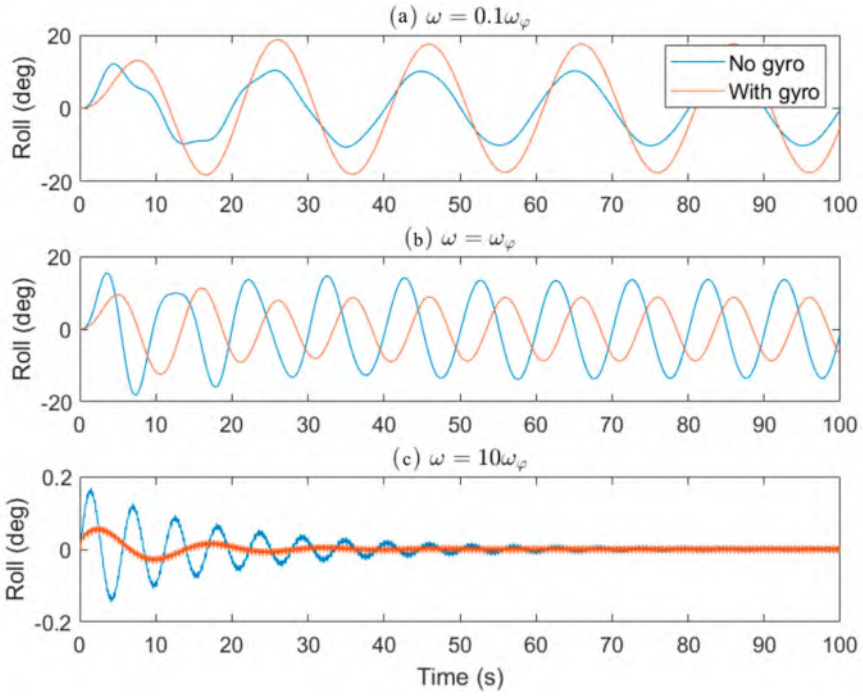

Figure 6. Roll responses under different wave frequencies with and without a gyrostabilizer.

In the low-frequency range, the gyrostabilizer significantly amplifies the roll response; a wave inclination of 10° can induce a maximum platform roll angle of 20°, which is undesirable. Near the natural frequency, the original platform exhibits a roll amplitude of approximately 15° under a 10° wave inclination. Although the gyrostabilizer reduces the response amplitude in this region, it introduces a noticeable phase lag. In the high-frequency range, the gyrostabilizer marginally increases the response amplitude; however,

the absolute magnitude remains small and has a negligible impact on platform safety. These results indicate that the controller design must suppress the additional low-frequency and high-frequency resonances introduced by the gyrostabilizer while simultaneously reducing the response amplitude near the natural frequency of the platform.

3.2. Analysis of Systems with an Active Controller

Based on the analysis in the previous section, an external control torque is introduced into the system and defined as

$$\tau_p = -k_p\beta - k_i\int \beta - k_d\dot{\beta}. \tag{26}$$

PID structure and tuning rationale: the proportional term shapes the effective restoring stiffness, the derivative term provides additional damping and suppresses the low-frequency resonance introduced by the passive gyro, and the integral term (if enabled) compensates slow bias/drift in measured roll angle. For the stability derivation below we set $k_i = 0$ to obtain a closed-form pole-placement condition for k_d; the final time-domain implementation can include a small ki with anti-windup when actuator saturation is present (Section 4.4).

Because β is a function of the platform roll angle φ, the feedback transfer function $H(s)$ after introducing the controller can be expressed as

$$H(s) = \frac{2(I\omega)^2 s^3}{Js^3 + k_d s^2 + (k_p + B_{gyro})s + k_i + C_{gyro}}. \tag{27}$$

Neglecting the integral gain k_i and substituting Equation (26) into the second equation of Equation (23), the simplified transfer function from φ to β is obtained as

$$H_{pr}(s) = \frac{\beta(s)}{\varphi(s)} = \left(\frac{I\omega}{J}\right)\left(\frac{s}{s^2 + \frac{B_g'}{J}s + \frac{C_g'}{J}}\right), \tag{28}$$

where $B_g^{'} = B_{gyro} + K_d$ and $C_g^{'} = C_{gyro} + K_p$.

The poles of the transfer function in Equation (28) are given by

$$p_{1,2} = -\frac{B_g'}{J} \pm \sqrt{\left(\frac{B_g'}{J}\right)^2 - 4\frac{C_g'}{J}}. \tag{29}$$

To ensure system stability, both poles must be real and negative. This condition is satisfied if and only if $\left(\frac{B_g'}{J}\right)^2 > 4\frac{C_g'}{J}$, $B_g' > 0$, $C_g' > 0$, which leads to the requirement $B_g' > \sqrt{4C_g'J}$. Accordingly, a constant $r > 1$ is introduced such that $B_g' = r\sqrt{4C_g'J}, r > 1$. The corresponding differential control gain is therefore obtained as

$$K_d = r\sqrt{4C_g'I_g} - B_g, r > 1 \tag{30}$$

After simplification, the closed-loop transfer function of the system can be obtained. The Bode plots of the original open-loop system, the system with a gyrostabilizer but without a controller, and the system with both a gyrostabilizer and an active controller are shown in Figure 7. The corresponding time-domain roll responses are shown in Figure 8. After introducing the active controller, the limitations associated with the passive gyrostabilizer are effectively mitigated. Platform swaying in both the low-frequency and high-frequency ranges is significantly suppressed, and the roll amplitude near the natural

frequency of the open-loop system is also substantially reduced. In addition, the phase lag introduced by the gyrostabilizer is considerably decreased, indicating improved dynamic performance and stability.

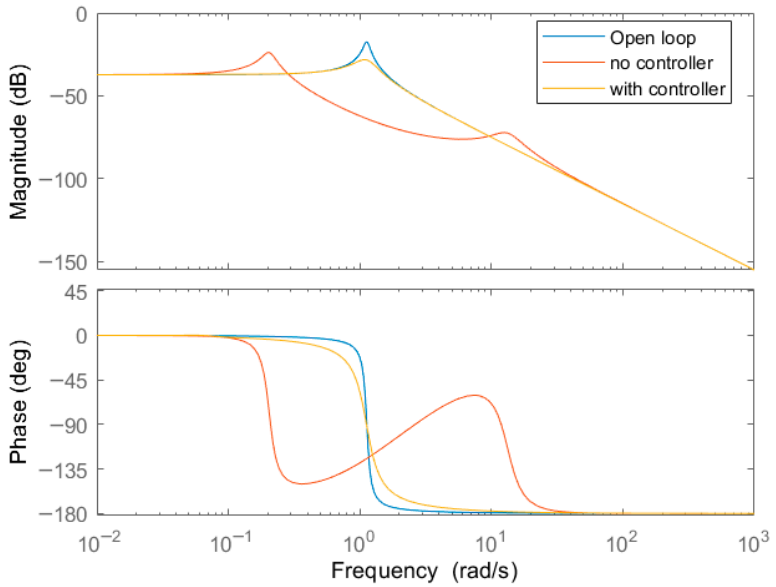

Figure 7. Bode plots of the original open-loop system, the system with a gyrostabilizer but without a controller, and the system with a gyrostabilizer and an active controller.

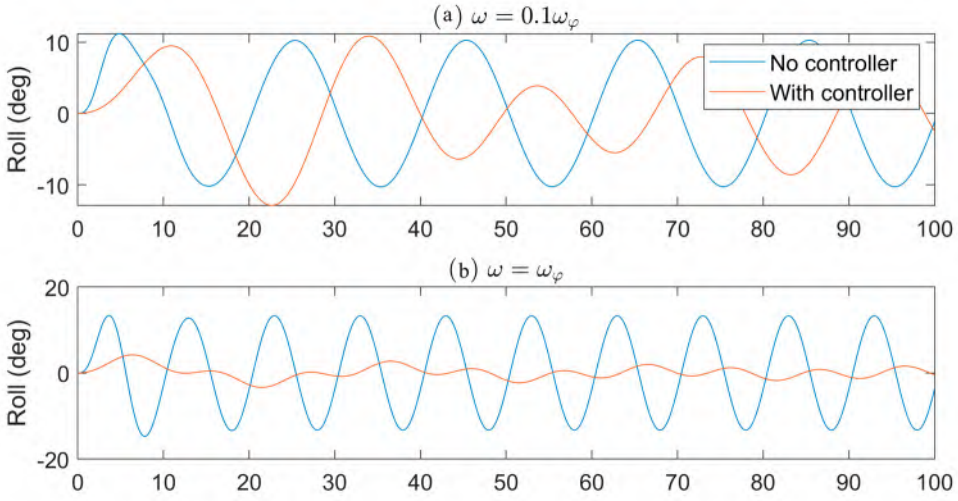

Figure 8. Roll responses under different wave frequencies with and without an active controller (both cases with a gyrostabilizer).

Discrete-time implementation: in practical systems the controller is executed digitally. The continuous-time feedback law can be discretized (e.g., Tustin) with sampling periods compatible with marine IMUs (typically 50–200 Hz). Sampling and sensor delay reduce phase margin; therefore, the chosen gains should preserve adequate robustness margins.

4. Results

Numerical simulations are conducted for the floating wind turbine platform equipped with a gyrostabilizer and an activated PID controller. The anti-rolling performance of this system is compared with that of (i) the baseline floating wind turbine platform without a gyrostabilizer and (ii) the platform equipped with a gyrostabilizer but without the PID controller activated. Time-domain simulations integrate the nonlinear roll

model (Equation (14)) while the controller gains are designed using the linearized model (Equation (15)), so that controller performance is assessed beyond the strict small-angle linearization used in the design stage.

Irregular waves are synthesized with random phases. Unless otherwise noted, the reported time traces correspond to a representative random-phase realization; for rigorous statistical confidence, multiple random seeds can be simulated and summarized using mean ± standard deviation of the reduction rate.

4.1. Anti-Rolling Effect at Different Rotational Speeds

Variations in the rotational moment of the gyrostabilizer lead to different levels of roll suppression for the floating wind turbine platform. In addition to adjusting the precession angular velocity, the rotor rotational speed can also be varied to achieve different anti-rolling effects.

Based on typical North Sea conditions, the significant wave height and peak period corresponding to moderate sea states are h = 6.0 m and T = 10.0 s, respectively. After applying Froude scaling, the corresponding model-scale parameters are h = 0.12 m and T = 1.414 s. Figure 9 shows the time-domain responses of the platform roll motion at different rotor speeds, both before and after activating the gyrostabilizer (with the gyroscope considered inactive when the rotor speed is zero). The results indicate that activating the gyrostabilizer effectively suppresses platform roll motion. As the rotor speed increases, the anti-rolling performance improves accordingly. Furthermore, when the PID controller is enabled, the suppression of roll motion is significantly enhanced compared with the passive gyrostabilizer configuration.

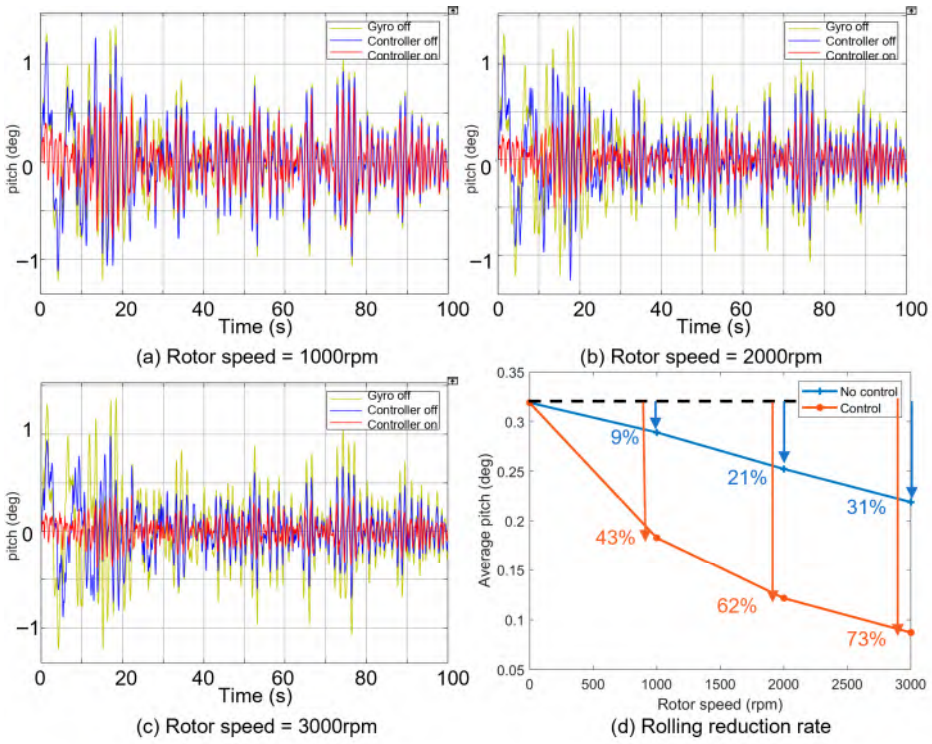

Figure 9. Time-domain roll responses of the floating wind turbine under different rotor speeds, showing the anti-rolling effect.

As shown in Figure 9, increasing the rotor speed leads to a continuous decrease in the average roll amplitude and a corresponding increase in the roll reduction rate. When the PID controller is not activated and the rotor speed reaches 3000 rpm, the average roll amplitude is reduced to 0.214°, corresponding to a reduction rate of 31%. After enabling

the PID controller at the same rotor speed, the average roll amplitude decreases further to 0.097°, with a roll reduction rate of 73%.

4.2. Anti-Rolling Effect at Different Wave Heights

For a fixed wave period of T = 10 s, wave heights of h = 2 m, 6 m, and 10 m are selected to represent calm, moderate, and extreme North Sea conditions, respectively. After applying Froude similarity scaling, the corresponding model-scale parameters are T = 1.414 s and h = 0.04 m, 0.12 m, and 0.2 m.

Figure 10 shows the time-domain roll responses of the platform before and after activating the PID-controlled gyrostabilizer, with the rotor operating at the rated speed of 2000 rpm. The results indicate that roll motion is reduced in both cases, with substantially improved performance when the PID controller is activated. In addition, the roll reduction effect becomes more pronounced as the wave height increases.

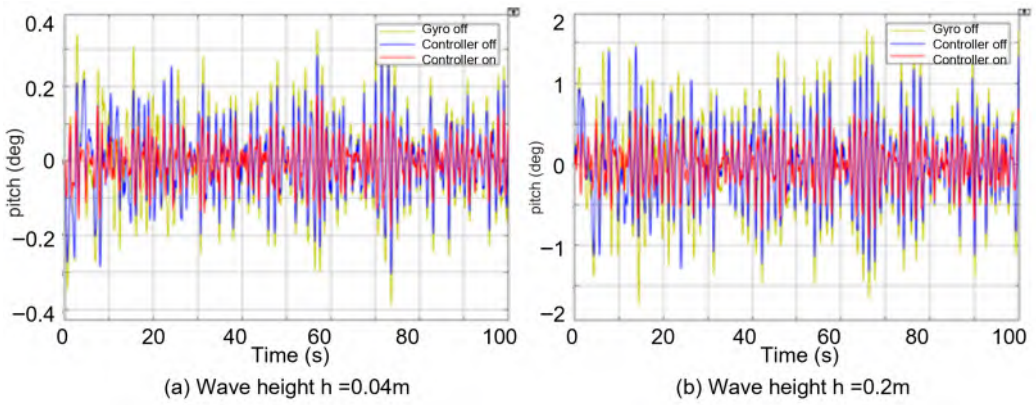

Figure 10. Time-domain roll responses of the floating wind turbine under different wave heights.

Figure 11 shows the reduction rates of the gyrostabilizer before and after activating the PID controller for different wave heights. Under the simulation conditions considered, the roll reduction rate increases continuously as the wave height rises from 0.04 m to 0.2 m. Without the PID controller, the reduction rate reaches 23% at a wave height of 0.20 m. After enabling the PID controller, the reduction rate increases significantly to 61% at the same wave height. These results indicate that the gyrostabilizer provides effective roll suppression across a range of wave heights. When the rotor speed and wave period are fixed, larger wave heights result in higher reduction rates. Moreover, the activation of the PID controller leads to a substantial improvement in anti-rolling performance compared with the passive gyrostabilizer configuration.

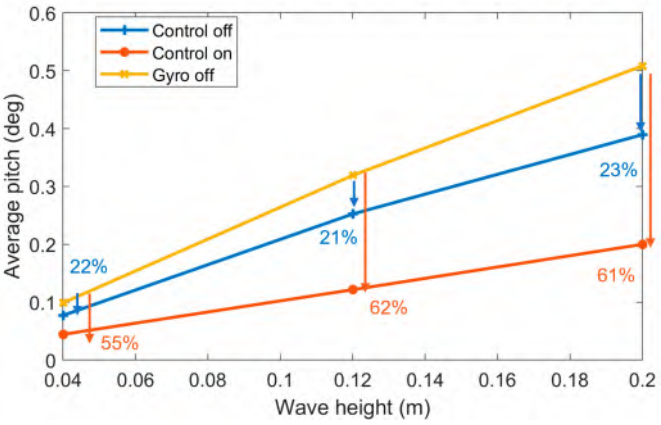

Figure 11. Damping effect of the gyroscope under different wave heights.

4.3. Anti-Rolling Effect at Different Wave Periods

For a fixed wave height of h = 6 m, wave periods of T = 5.5 s, 10 s, and 12.5 s are selected to represent low-, medium-, and high-frequency sea states in the North Sea. After scaling according to the Froude similarity criterion, the corresponding model-scale parameters are h = 0.12 m and T = 0.78 s, 1.414 s, and 1.77 s.

Figure 12 shows the time-domain roll responses of the floating wind turbine platform before and after activating the PID-controlled gyrostabilizer, with the rotor operating at the rated speed of 2000 rpm. The results show that roll motion is reduced in both cases, with noticeably better suppression when the PID controller is enabled. In addition, the roll reduction effect improves as the wave period increases.

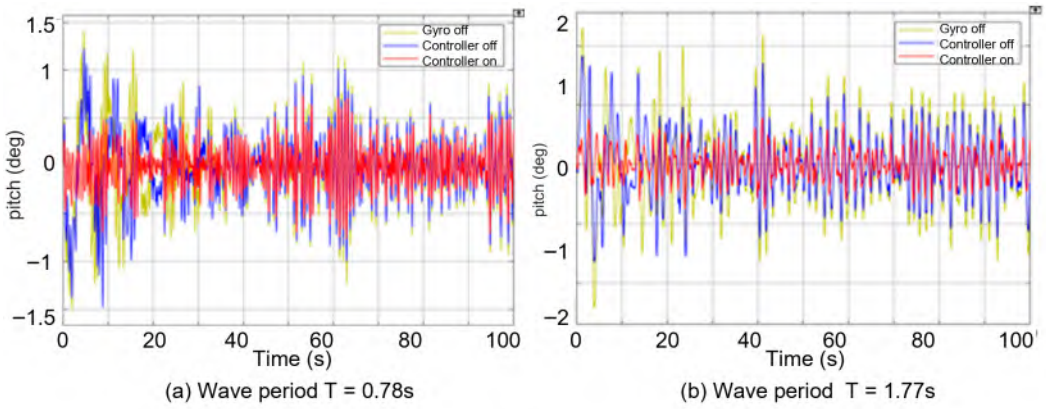

Figure 12. Time-domain roll responses of the floating wind turbine under different wave periods.

Figure 13 shows the roll reduction rates of the gyrostabilizer before and after activating the PID controller for different wave periods. As the wave period increases from 0.78 s to 1.77 s, the roll reduction rate increases continuously. Without the PID controller, the reduction rate reaches 22% at the longest wave period. After enabling the PID controller, the reduction rate increases substantially to 63% under the same conditions. These results indicate that the gyrostabilizer achieves effective roll suppression across a range of wave periods. When the rotor speed and wave height are fixed, longer wave periods lead to higher reduction rates. Compared with the passive gyrostabilizer configuration, the PID-controlled gyrostabilizer provides significantly improved anti-rolling performance.

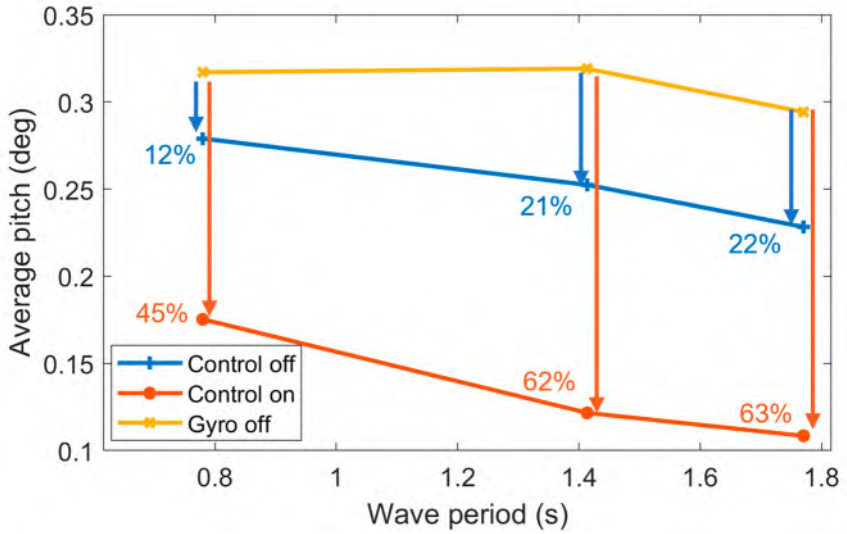

Figure 13. Damping effect of the gyroscope under different wave periods.

4.4. Practical Implementation Considerations and Extended Discussion

Sea-state transitions: in practice, sea states vary with time. The proposed feedback controller does not require wave preview, hence it can respond immediately to changes in measured roll motion. A sea-state transition test can be carried out by switching the JONSWAP parameters (Hs, Tp) during simulation and evaluating transient roll suppression and actuator effort.

Power and feasibility estimate: the actively controlled gyro requires (i) rotor spin power to overcome mechanical/electrical losses and (ii) precession-actuator power to generate the commanded control torque. While the rotor kinetic energy is large, maintaining constant speed primarily compensates for losses; the incremental control power is dominated by the precession actuator and can be bounded by $Pc(t) = |u(t)\cdot\beta(t)|$. With the imposed precession-rate limit $\beta_{max} = 1.1$ rad/s and a conservative bound on the control torque umax chosen from the maximum disturbance moment required in Section 2.4, an upper-bound estimate $P_{c,max} = u_{max}\ \beta_{max}$ can be computed and compared to the turbine power. This manuscript reports the resulting order-of-magnitude ratio and emphasizes that detailed actuator-loss modeling is platform-specific.

Physical constraints: in addition to the precession-rate cap, practical designs impose a finite precession-angle range $\beta \in [-\beta_{max}, \beta_{max}]$ due to mechanical end-stops and cable routing. The controller should therefore include saturation and anti-windup logic; otherwise, large transient waves or sea-state transitions may cause integrator windup and performance degradation. These constraints do not change the frequency-domain conclusions but affect achievable reduction rates in extreme conditions.

Limitations: the present model focuses on 1-DOF roll under beam seas and neglects coupled aero-hydro-servo-elastic effects of the turbine/tower. It also assumes simplified hydrodynamic coefficients and unidirectional (long-crested) irregular waves. These simplifications help isolate the roll-stabilization mechanism but should be relaxed in future work using fully coupled 6-DOF tools and multi-directional spectra. In addition, the dual-gyro derivation assumes ideal symmetry; small mismatches in rotor speed or inertia may introduce residual interference moments and should be quantified in future work. Similarly, oblique seas and multi-directional spectra may excite additional DOFs and coupling effects.

5. Conclusions

This study develops a comprehensive dynamic model that integrates wave excitation, platform dynamics, and gyrostabilizer behavior, and proposes an active control strategy for suppressing the swaying motion of floating wind turbine platforms. The influences of rotor speed, wave height, and wave period on roll-damping performance are investigated. Through stability analysis and numerical simulations, the damping effectiveness of the gyrostabilizer on floating wind turbine platforms is evaluated.

By regulating the platform roll angle, the gyroscope precession angle can be effectively controlled. This approach enables not only the regulation of the precession amplitude of the gyroscope rotation axis but also the determination of an optimal precession angular velocity through the established relationship between roll motion and gyroscopic precession. The proposed controller exhibits a pronounced damping effect under a wide range of irregular wave conditions.

After activating the PID controller, the damping performance of the gyrostabilizer increases consistently with increasing rotor speed, wave height, and wave period. Compared with a passive gyrostabilizer configuration, the introduction of active control results in a substantial improvement in roll-suppression capability.

Author Contributions: Conceptualization, P.C. and T.Z.; methodology, P.C.; software, T.Z.; validation, T.Z. and W.Z.; formal analysis, T.Z. and W.Z.; investigation, P.C. and T.Z.; resources, T.Z.; data curation, W.Z.; writing—original draft preparation, P.C.; writing—review and editing, W.Z.; visualization, W.Z.; supervision, D.W.; project administration, P.C.; funding acquisition, P.C. All authors have read and agreed to the published version of the manuscript.

Funding: This work was supported by the National Natural Science Foundation of China (52301328).

Data Availability Statement: The original contributions presented in this study are included in the article. Further inquiries can be directed to the corresponding author.

Conflicts of Interest: The authors declare no conflicts of interest.

References

1. Wang, C.M.; Utsunomiya, T.; Wee, S.C.; Choo, Y.S. Research on floating wind turbines: A literature survey. *IES J. Part A Civ. Struct. Eng.* **2010**, *3*, 267–277. [CrossRef]
2. Ou, J.; Long, X.; Li, Q.S.; Xiao, Y.Q. Vibration control of steel jacket offshore platform structures with damping isolation systems. *Eng. Struct.* **2007**, *29*, 1525–1538. [CrossRef]
3. McMorland, J.; Collu, M.; McMillan, D.; Carroll, J. Operation and maintenance for floating wind turbines: A review. *Renew. Sustain. Energy Rev.* **2022**, *163*, 112499. [CrossRef]
4. Bashetty, S.; Ozcelik, S. Review on dynamics of offshore floating wind turbine platforms. *Energies* **2021**, *14*, 6026. [CrossRef]
5. Jonkman, J.M.; Matha, D. Dynamics of offshore floating wind turbines—Analysis of three concepts. *Wind Energy* **2011**, *14*, 557–569. [CrossRef]
6. Jonkman, J.M. Dynamics of offshore floating wind turbines—Model development and verification. *Wind Energy* **2009**, *12*, 459–492. [CrossRef]
7. Yap, Z.H.; Tang, C.H.H.; Kang, H.S.; Quen, L.K.; Nur, T. Roll motion compensation by active marine gyrostabiliser. *Indian J. Geo-Mar. Sci. (IJMS)* **2022**, *50*, 922–929.
8. Palraj, M.; Rajamanickam, P. Motion control of a barge for offshore wind turbine (OWT) using gyrostabilizer. *Ocean Eng.* **2020**, *209*, 107500. [CrossRef]
9. Palraj, M.; Rajamanickam, P. Motion control studies of a barge mounted offshore dynamic wind turbine using gyrostabilizer. *Ocean Eng.* **2021**, *237*, 109578. [CrossRef]
10. Hu, L.; Zhang, M.; Yu, X.; Yuan, Z.M.; Li, W. Real-time control of ship's roll motion with gyrostabilisers. *Ocean Eng.* **2023**, *285*, 115348. [CrossRef]
11. Fenu, B.; Attanasio, V.; Casalone, P.; Novo, R.; Cervelli, G.; Bonfanti, M.; Sirigu, S.A.; Bracco, G.; Mattiazzo, G. Analysis of a gyroscopic-stabilized floating offshore hybrid wind-wave platform. *J. Mar. Sci. Eng.* **2020**, *8*, 439. [CrossRef]
12. Perez, T.; Steinmann, P.D. Analysis of ship roll gyrostabiliser control. *IFAC Proc. Vol.* **2009**, *42*, 310–315. [CrossRef]
13. Song, K.-S.; Kim, S.-M.; Kwak, M.K.; Zhu, W. Development of a control algorithm for active control of rolling motion of a ship using a gyrostabilizer. *Ocean Eng.* **2023**, *280*, 114669. [CrossRef]
14. Qi, Z.G.; Sun, W.X.; Chen, Y.; Zhao, W. Research on the ship roll stabilization with gyro-Stabilizerat low forward speed. In *Proceedings of the 37th China Control Conference, Wuhan, China, 25–27 July 2018*; IEEE: New York, NY, USA, 2018; pp. 486–490.
15. Didier, F.; Liu, Y.-C.; Laghrouche, S.; Depernet, D. A Comprehensive Review on Advanced Control Methods for Floating Offshore Wind Turbine Systems above the Rated Wind Speed. *Energies* **2024**, *17*, 2257. [CrossRef]
16. Amouzadrad, P.; Mohapatra, S.C.; Guedes Soares, C. Review on Sensitivity and Uncertainty Analysis of Hydrodynamic and Hydroelastic Responses of Floating Offshore Structures. *J. Mar. Sci. Eng.* **2025**, *13*, 1015. [CrossRef]
17. Walker, K.L.; Jordan, L.B.; Giorgio-Serchi, F. Nonlinear model predictive dynamic positioning of a remotely operated vehicle with wave disturbance preview. *Int. J. Rob. Res.* **2025**, *44*, 932–951. [CrossRef]
18. de Oliveira, É.L.; de Barros, E.A. Acceleration based control strategies applied to ROV station keeping under wave disturbance. *Ocean Eng.* **2025**, *342*, 122871. [CrossRef]
19. Walker, K.L.; Stokes, A.A.; Kiprakis, A.; Giorgio-Serchi, F. Feed-forward disturbance compensation for station keeping in wave-dominated environments. In *Proceedings of the OCEANS 2023–Limerick, Limerick, Ireland, 5–8 June 2023*; IEEE: New York, NY, USA, 2023.
20. Hegazy, A.; Naaijen, P.; Leroy, V.; Bonnefoy, F.; Mojallizadeh, M.R.; Pérignon, Y.; van Wingerden, J.-W. The potential of wave feedforward control for floating wind turbines: A wave tank experiment. *Wind Energ. Sci.* **2024**, *9*, 1669–1688. [CrossRef]
21. Cheng, P.; Shen, J.; Zhang, T.; Wan, D. Simulating the stability of a semi-submersible wind turbine platform equipped with gyroscopic stabilizers. In Proceedings of the ISOPE International Ocean and Polar Engineering Conference, Seoul, Republic of Korea, 1–6 June 2025; ISOPE-I-25-036; ISOPE: Mountain View, CA, USA, 2025.

22. Robertson, A.; Jonkman, J.; Masciola, M.; Song, H.; Goupee, A.; Coulling, A.; Luan, C. *Definition of the Semisubmersible Floating System for Phase II of OC4*; NREL Technical Report; NREL/TP-5000-60601; National Renewable Energy Laboratory: Golden, CO, USA, 2014.
23. Dagher, H.; Viselli, A.; Goupee, A.; Allen, C. *1:50 Scale Testing of Three Floating Wind Turbines at MARIN and Numerical Model Validation Against Test Data*; Technical Report; University of Maine: Orono, ME, USA, 2017.
24. Robertson, A.; Jonkman, J.; Wendt, F.; Goupee, A.; Dagher, H. *Definition of the OC5 DeepCwind Semisubmersible Floating System (Phase II)*; Technical Report; National Renewable Energy Laboratory: Golden, CO, USA, 2016.
25. Soleymani, M.; Norouzi, M. Active gyroscopic stabilizer to mitigate vibration in a multimegawatt wind turbine. *Wind Energy* **2021**, *24*, 720–736. [CrossRef]
26. Pesman, E.; Bayraktra, D.; Taylan, M. Influence of damping on the roll motion of ships. In *Proceedings of the 2nd International Conference on Marine Research and Transportation, Naples, Italy, 28–30 June 2007*; ICMRT: Lucknow, India, 2007; pp. 127–133.
27. Surendran, S.; Lee, S.K.; Reddy, J.V.R.; Lee, G. Non-linear roll dynamics of a Ro-Ro ship in waves. *Ocean Eng.* **2005**, *32*, 1818–1828. [CrossRef]